

THE EFFECT OF MAGNETIC FIELD TILT AND DIVERGENCE ON THE MASS FLUX AND FLOW SPEED IN A LINE-DRIVEN STELLAR WIND

STANLEY P. OWOCKI

Bartol Research Institute, University of Delaware, Newark, DE 19716

AND

ASIF UD-DOULA

Department of Physics, North Carolina State University, Box 8202, Raleigh, NC 27695-8202

Received 2003 August 25; accepted 2003 September 23

ABSTRACT

We carry out an extended analytic study of how the tilt and faster-than-radial expansion from a magnetic field affect the mass flux and flow speed of a line-driven stellar wind. A key motivation is to reconcile results of numerical MHD simulations with previous analyses that had predicted nonspherical expansion would lead to a strong speed enhancement. By including finite-disk correction effects, a dynamically more consistent form for the nonspherical expansion, and a moderate value of the line-driving power index α , we infer more modest speed enhancements that are in good quantitative agreement with MHD simulations and also are more consistent with observational results. Our analysis also explains simulation results that show the latitudinal variation of the surface mass flux scales with the square of the cosine of the local tilt angle between the magnetic field and the radial direction. Finally, we present a perturbation analysis of the effects of a finite gas pressure on the wind mass-loss rate and flow speed in both spherical and magnetic wind models, showing that these scale with the ratio of the sound speed to surface escape speed, a/v_{esc} , and are typically 10%–20% compared to an idealized, zero-gas-pressure model.

Subject headings: MHD — stars: early-type — stars: magnetic fields — stars: mass loss — stars: winds, outflows

1. INTRODUCTION

In a recent paper (ud-Doula & Owocki 2002, hereafter UO02), we presented numerical magnetohydrodynamic (MHD) simulations of the effect of a stellar dipole magnetic field on the line-driven stellar wind from a nonrotating, hot, luminous star. We showed that the overall influence of the field on the wind depends largely on a single, dimensionless, “wind magnetic confinement parameter” η_* ($=B_{\text{eq}}^2 R_*^2 / M v_{\infty}$), which characterizes the ratio between magnetic field energy density and wind kinetic energy density. Because the field energy declines faster than the wind energy, in the outer regions the magnetic field is always dominated by the radial wind outflow, which thus asymptotically stretches the field into a radial configuration, regardless of the strength of η_* . For weak confinement $\eta_* < 1$, this radial opening of the field applies throughout the whole computational domain. But for stronger confinement $\eta_* > 1$, the magnetic field remains closed near the surface and over a limited range of latitude around the magnetic equator.

In this paper we provide further analysis and interpretation of how key wind properties, namely, the surface mass flux and asymptotic flow speed (see Figs. 1*a* and 1*b*), are modified by the presence of a magnetic field. One central motivation is to reconcile results of our numerical MHD simulations with the previous scaling analysis done by MacGregor (1988, hereafter M88), which had predicted that the faster-than-radial divergence of magnetic flux tubes would lead to substantial (factor of 3–4) increase in the terminal velocity of a line-driven wind, compared to that of the nonmagnetic, spherical-expansion case. Since the implied flow speeds ranging up to 5000–6000 km s^{−1} are never observed through blue edges of UV P Cygni lines from hot stars (Prinja & Howarth 1986; Howarth & Prinja 1989), that prediction could be a basis for inferring that hot stars lack magnetic fields with sufficient strength to substantially influence their stellar winds.

Here we develop (§ 3) a simplified formulation of the one-dimensional equations for a steady line-driven wind. Applying this to cases with faster-than-radial area expansion (§ 4), we show that the prediction of a threefold increase in flow speed is the consequence of certain assumptions and idealizations (point-star radiation, phenomenological flow expansion, and large line power index α) in the previous M88 analysis; when these assumptions are relaxed (to include finite-disk correction, a dynamical flow divergence, and more realistic α), the expected effect on flow speeds is consistent with the more modest $\lesssim 50\%$ increase typically found in our MHD simulations. We further show that the inferred simulation scaling of the base mass flux with the square of the cosine of the surface field tilt angle can be understood from a simple modified one-dimensional tilted flow analysis (§ 5). After a brief discussion of the implications for stellar wind structure (§ 6), we conclude with a summary (§ 7) of our main results.

2. SUMMARY OF KEY RESULTS OF TWO-DIMENSIONAL MHD SIMULATIONS

Figures 1*a* and 1*b* summarize two key results of our two-dimensional MHD simulations, wherein we study the dynamical competition between magnetic field and wind by inserting a dipole magnetic field of varied strength (parameterized by η_*) into a previously relaxed, spherically symmetric, Castor, Abbott, & Klein (1975, hereafter CAK) wind.¹ For the asymptotic states when the regions of magnetic field opened by the

¹ The simulation results given here are analogous to those presented by UO02 and ud-Doula (2002) but correct a minor coding error that leads the polar flow to have an artificially enhanced mass flux and an artificially reduced flow speed. As in UO02, the model here is assumed isothermal, with a constant sound speed $a = 26.3$ km s^{−1}, implying a ratio $s \equiv a^2/v_{\text{esc}}^2 = 0.0014$ between the gas internal energy and surface escape energy. See § 3 and Appendices A and B.

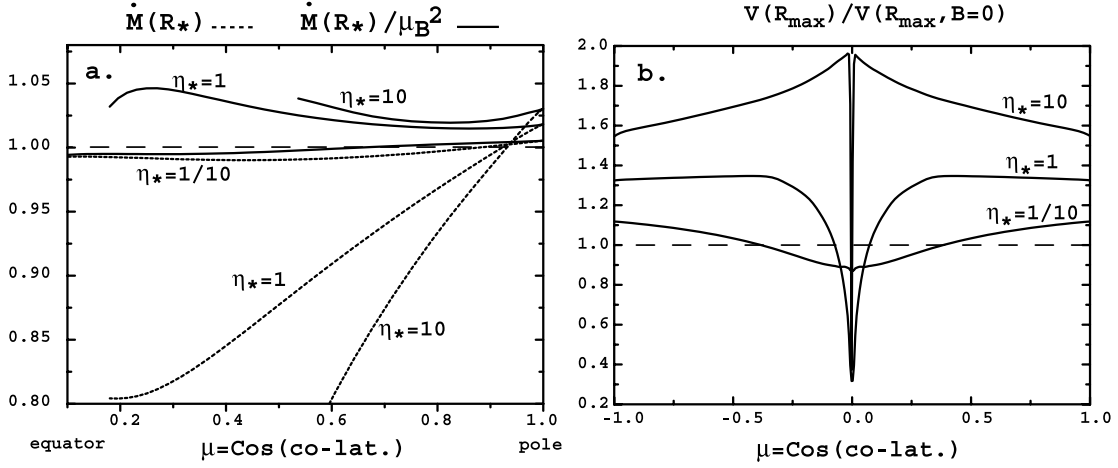


FIG. 1.—(a) Latitudinal variation of the base mass flux in open field regions of the two-dimensional MHD simulations. The dotted curves represent the mass flux scaled by the corresponding spherical model. The solid curves add an additional scaling by μ_B^2 , where $\mu_B \equiv \hat{\mathbf{B}}_* \cdot \hat{\mathbf{r}}$ is the radial projection of a unit vector along the base magnetic field. (b) Latitudinal variation of the flow speed at the maximum radius $R_{\text{max}} = 6R_*$ of these same two-dimensional MHD simulations, scaled by the corresponding speed in the spherical, nonmagnetic ($B = 0$) model.

wind have a nearly steady state flow, both figures show results for three cases, with the degree of magnetic confinement ranging from weak ($\eta_* = 0.1$), through moderate ($\eta_* = 1$), to strong ($\eta_* = 10$).

In Figure 1a the dotted curves show the latitudinal variation of the base mass flux, while the solid curves show this same flux scaled by μ_B^2 , where μ_B is the radial projection of a unit vector along the base magnetic field. The near constancy of this scaled flux is explained in § 5, which uses a simple tilted-flow analysis of the base line-driving to show that the radial mass flux does indeed vary with the square of the field's radial projection cosine, $\dot{M} \sim \mu_B^2$.

At the magnetic poles, the radial orientation of the field means the flow is also radial, with essentially the same base mass flux as in the spherical model.²

Figure 1b plots the latitudinal variation of the flow speed at the maximum model radius $R_{\text{max}} = 6R_*$, scaled by the corresponding speed in the spherical, nonmagnetic ($B = 0$) model. The lower speeds toward the magnetic equator ($\mu \approx 0$) reflect the various relative degrees of equatorial flow compression, which increases the density and so reduces the radiative acceleration. In the highest magnetic confinement case $\eta_* = 10$, the increased speeds at midlatitudes ($0.1 < |\mu| < 0.8$) result from a combination of the reduced mass flux and greater flow expansion, both of which reduce the density and so increase the radiative acceleration.

While such latitudinal trends thus make sense qualitatively, our focus below will be on developing a semiquantitative understanding of the wind properties at the magnetic poles, where the radial orientation of the flow makes possible a one-dimensional analysis, if one takes proper account of the nonspherical expansion of the flow area. This was essentially the approach taken by M88, but the factor 3 or more speed enhancements found there are substantially greater than those in Figure 1b, which even for the strongest magnetic confinement $\eta_* = 10$ shows a polar speed enhancement of only 1.54.

The next two sections develop and apply a formalism for understanding this difference.

3. FLOW ANALYSES FOR SPHERICAL EXPANSION

3.1. CAK Model of a Wind Driven by a Point Source of Radiation

To provide a basis for our analysis of how the tilt and areal divergence of a magnetic field modify a wind outflow, let us first recast the basic CAK formalism in a somewhat more tractable, physically transparent form. First, for a steady, one-dimensional stellar wind driven radially by line-scattering of radiation from a central point source, the associated equation of motion for the radial velocity v as a function of radius r takes the form

$$\left(1 - \frac{a^2}{v^2}\right) v \frac{dv}{dr} = -\frac{GM(1 - \Gamma)}{r^2} + g_{\text{CAK}} + \frac{2a^2}{r}, \quad (1)$$

where $GM(1 - \Gamma)/r^2$ is the effective gravitational acceleration and the Eddington parameter $\Gamma \equiv \kappa_e L / 4\pi G M c$ accounts for the effect of electron scattering opacity κ_e interacting with the stellar luminosity L , with c the speed of light. The factor in parentheses on the left-hand side with the sound speed a accounts for gas pressure effects that allow for smooth mapping of the wind outflow onto a hydrostatic atmosphere below the sonic point, where $v = a$. On the right-hand side the flow's areal expansion also gives rise to a pressure-form term $2a^2/r$, which compared to the competing gravitational term is of order $s \equiv (a/v_{\text{esc}})^2 \approx 0.001$, where $v_{\text{esc}} \equiv [2GM(1 - \Gamma)/R_*]^{1/2}$ is the effective escape speed from the stellar surface radius R_* . The outward driving against gravity through the sonic point and beyond must thus be principally via the line acceleration, which under CAK's original assumption of radially streaming radiation from a point source can be written as

$$g_{\text{CAK}} = \frac{1}{(1 - \alpha)} \frac{\kappa_e L}{4\pi r^2 c} \left(\frac{dv/dr}{\rho c} \frac{\bar{Q}}{\bar{Q}_{\kappa_e}} \right)^\alpha, \quad (2)$$

where ρ is the density and α is the CAK exponent. Here the line normalization \bar{Q} is related to the usual CAK k -parameter

² The few percent increase is a second-order effect, associated with the finite sound speed and the resulting detachment of the flow critical point from the surface, where faster areal expansion reduces the density and so allows driving of a somewhat greater mass flux. See Appendix B.

through $k = \bar{Q}^{1-\alpha} (v_{\text{th}}/c)^\alpha / (1 - \alpha)$ but offers the advantages of being a dimensionless measure of line opacity that is independent of the assumed ion thermal speed v_{th} , with a nearly constant characteristic value of order $\bar{Q} \sim 10^3$ for a wide range of ionization conditions (Gayley 1995).

To proceed, let us define the gravitationally scaled inertial acceleration

$$w' \equiv \frac{r^2 v dv/dr}{GM(1 - \Gamma)}. \quad (3)$$

In terms of an inverse radius coordinate $x \equiv 1 - R_*/r$, note that $w' = dw/dx$, where $w \equiv v^2/v_{\text{esc}}^2$ represents the ratio of wind kinetic energy to the effective gravitational binding $v_{\text{esc}}^2/2 \equiv GM(1 - \Gamma)/R_*$ from the stellar surface radius R_* . We can then rewrite the equation of motion (1) in the dimensionless form

$$\left(1 - \frac{s}{w}\right) w' = -1 + C(w')^\alpha + \frac{2s}{(1-x)}, \quad (4)$$

where $s \equiv a^2/v_{\text{esc}}^2$ and we have eliminated the density ρ in favor of the mass-loss rate $\dot{M} = 4\pi r^2 \rho v$ for the assumed steady, spherical expansion, with the line-force constant defined by

$$C \equiv \frac{1}{1 - \alpha} \left(\frac{L}{\dot{M} c^2}\right)^\alpha \left(\frac{\bar{Q}\Gamma}{1 - \Gamma}\right)^{1-\alpha}. \quad (5)$$

Note that for fixed sets of parameters for the star (L , M , Γ) and line-opacity (α , \bar{Q}), this constant scales with the mass-loss rate as $C \sim 1/\dot{M}^\alpha$.

The essential elements of interest in this paper can be analyzed without including the small gas-pressure terms, and so we shall henceforth consider only the limit of vanishing sound speed $a \sim \sqrt{s} \rightarrow 0$. (The corrections from a small but finite s are examined in Appendices A and B.) For this limit, Figure 2 illustrates a graphical solution to equation (4) for various values of C . For high \dot{M} or small C there are no solutions, while for small \dot{M} or high C there are two solutions. The CAK critical solution corresponds to a *tangential* intersection between line force and combined inertia plus gravity, for which

$$\alpha C_c w_c'^{\alpha-1} = 1 \quad (6)$$

and thus

$$w_c' = \frac{\alpha}{1 - \alpha}, \quad (7)$$

with

$$C_c = \frac{1}{\alpha^\alpha (1 - \alpha)^{1-\alpha}}. \quad (8)$$

Applying this in equation (5), we can then solve for the mass-loss rate, yielding the standard CAK scaling

$$\dot{M}_{\text{CAK}} = \frac{L}{c^2} \frac{\alpha}{1 - \alpha} \left(\frac{\bar{Q}\Gamma}{1 - \Gamma}\right)^{(1-\alpha)/\alpha}. \quad (9)$$

Moreover, since the scaled equation of motion (4) has no explicit spatial dependence, the scaled critical acceleration w_c' applies throughout the wind. This can thus be trivially

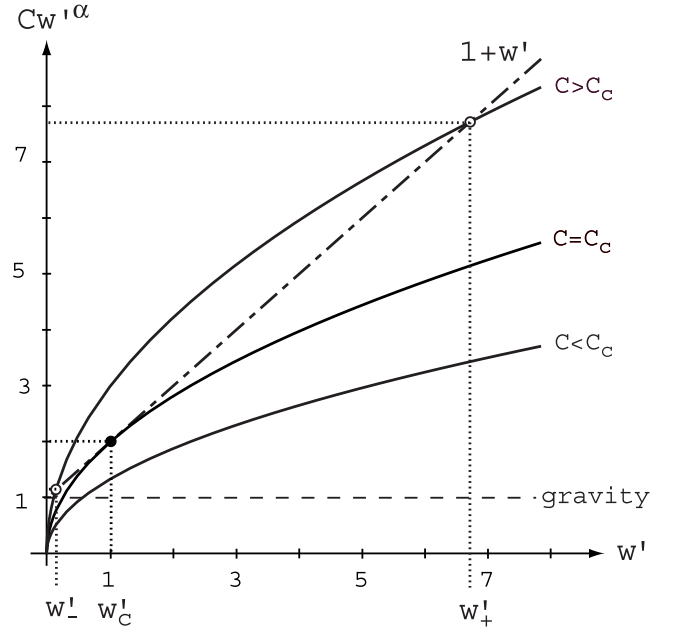


FIG. 2.—Graphical solution of the dimensionless equation of motion (4) representing a one-dimensional, point-star, zero-sound-speed CAK wind, as controlled by the constant $C \sim 1/\dot{M}^\alpha$, which determines the intersections of the line force Cw'^α (solid lines) with the combined gravity plus inertia $1 + w'$ (dot-dashed lines). If \dot{M} is too big, there are no solutions; if \dot{M} is small there are two solutions. A maximal value $\dot{M} = \dot{M}_{\text{CAK}}$ defines a single, “critical” solution.

integrated to yield $w = \alpha x / (1 - \alpha)$, which is equivalent to the CAK velocity law

$$v(r) = v_\infty \left(1 - \frac{R_*}{r}\right)^{1/2}, \quad (10)$$

where the wind terminal speed $v_\infty = v_{\text{esc}} [\alpha / (1 - \alpha)]^{1/2}$ scales with $v_{\text{esc}} \equiv [2GM(1 - \Gamma)/R_*]^{1/2}$, the effective escape speed from the stellar surface radius R_* .

3.2. The Finite-Disk Correction Factor

The above analysis has so far been based on the idealization of radially streaming radiation, as if the star were a point source at the origin. This was the basis of the original CAK wind solutions, although they did already identify (but did not implement) the appropriate “finite-disk correction factor” to account for the full angular extent of the star (see CAK eq. [50]),

$$f_d = \frac{(1 + \sigma)^{1+\alpha} - (1 + \sigma\mu_*^2)^{1+\alpha}}{(1 + \alpha)\sigma(1 + \sigma)^\alpha(1 - \mu_*^2)}, \quad (11)$$

where $\sigma \equiv (r/v) dv/dr - 1$ and $\mu_*^2 \equiv 1 - R_*^2/r^2$. When this factor is included to modify the point-star CAK line acceleration (eq. [2]), its complex dependence on radius, velocity, and velocity gradient complicates somewhat the solution of the full equation of motion (1). But full solutions have been derived independently by Friend & Abbott (1986) and Pauldrach, Puls, & Kudritzki (1986). They yield a somewhat reduced mass-loss rate $\dot{M}_{\text{fd}} \approx \dot{M}_{\text{CAK}} / (1 + \alpha)^{1/\alpha}$, higher terminal speed $v_\infty \approx 3v_{\text{esc}}$, and flatter velocity law, roughly characterized by replacing the exponent $\frac{1}{2}$ in equation (10) with a somewhat higher value $\beta \approx 0.8$.

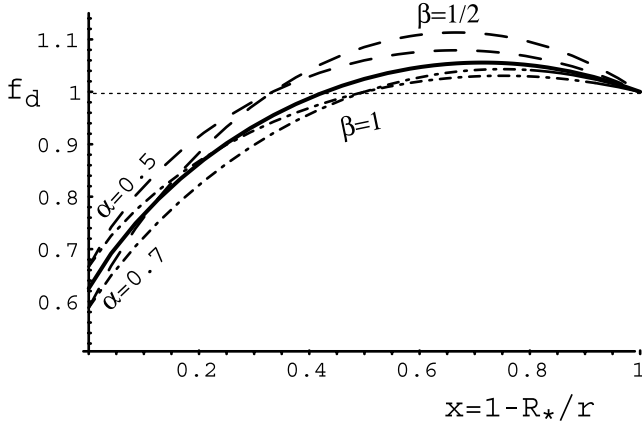


FIG. 3.—Spatial variation of the finite-disk correction factor f_d , plotted vs. scaled inverse radius $x = 1 - R_*/r$ for various CAK exponents α and velocity-law exponents β . The heavy solid curve shows our standard case with $\alpha = 0.6$ and $\beta = \frac{3}{4}$. The dashed curves use $\beta = \frac{1}{2}$, the dot-dashed curves use $\beta = 1$, and they are each plotted for CAK exponents $\alpha = 0.5$ and $\alpha = 0.7$ that span the nominal range. A key point is that all these varied curves have a similar form, rising sharply from a base value [$f_{d*} = 1/(1 + \alpha)$], crossing above unity (dotted line), and then relaxing back to it at large radial distances, $x \rightarrow 1$.

If one simply assumes such a canonical β velocity law, Figure 3 illustrates the specific spatial variations of $f_d(x)$ for various CAK exponents α and velocity exponents β . All these varied cases show a quite common general behavior. For the initial acceleration from a static stellar surface ($r \approx R_*$, or $x \rightarrow 0$; where $v \rightarrow 0$ with finite dv/dr , implying $\sigma \rightarrow \infty$), f_d has a starting value $f_{d*} \approx 1/(1 + \alpha)$. It then increases outward, past unity at the point where the wind has a locally isotropic expansion (with $dv/dr = v/r$, so that $\sigma = 0$), and then finally falls back asymptotically toward unity at large radii ($x \rightarrow 1$), where the star is indeed well approximated by a point source.

To understand the dynamical effect of this finite-disk factor, and indeed to see how it interacts with effects of a magnetic field, it is helpful to examine how such a typical radial variation influences the scaled acceleration w' through solutions to the appropriately modified equation of motion (cf. eq. [4]),

$$w' = -1 + fC_*(w')^\alpha, \quad (12)$$

where for convenience we have defined scaled quantities $f \equiv f_d/f_{d*}$ and $C_* \equiv f_{d*}C$ and, for simplicity, again taken the zero-sound-speed limit $s = 0$. Since f increases outward from unity at the surface, the surface radius $r = R_*$ ($x = 0$) now represents a critical point (also known as a “choke” or “throat”) that fixes the required minimal value of $C_* = C_c = 1/\alpha^\alpha (1 - \alpha)^{1-\alpha}$ to allow an accelerating solution from this wind base. Accounting then for the mass-loss rate scaling of $C_* \sim 1/\dot{M}^\alpha$, we readily see that the net result is to reduce the maximal allowed mass loss to

$$\dot{M}_{fd} = f_{d*}^{1/\alpha} \dot{M}_{CAK} = \frac{\dot{M}_{CAK}}{(1 + \alpha)^{1/\alpha}}. \quad (13)$$

This thus provides a simple rationale for this aspect of the detailed numerical solutions of Friend & Abbott (1986) and Pauldrach et al. (1986).

As the finite-disk factor increases from its reduced base value, the lower mass loading allows for stronger CAK line

force, with now the resulting greater acceleration being “leveraged” by its effect in further increasing the line force. From the graphical solution in Figure 2, one sees that a modest increase in the line-acceleration term $[C(w')^\alpha]$ above the critical solution (with $C = C_c$) leads to a solution with a *much* larger scaled acceleration w' . (There also arises a much shallower acceleration, but as discussed by Feldmeier, Shlosman, & Hamann [2002], maintaining this beyond the critical point requires a special kind of outer boundary condition, whereas the more rapid acceleration is compatible with the standard assumption of simple expansion into a vacuum.)

Figure 4 illustrates this strong sensitivity to the finite-disk correction in terms of $\sqrt{w'}$, which sets the scaling of terminal speed $v_\infty \sim v_{esc} \sqrt{w'}$. Note how a modest, less than a factor of 2 change in f leads to large increases in this speed scale $\sqrt{w'}$, with the trends being most dramatic for the largest α . From equation (12), we see that in the limit of large acceleration $w' \gg 1$, the speed scaling approaches the form

$$\sqrt{w'} \sim (C_c f)^{1/2(1-\alpha)}, \quad w' \gg 1, \quad (14)$$

which is illustrated through the dashed curves in Figure 4. For the specific case $\alpha = \frac{1}{2}$, we can use the quadratic formula to obtain a simple expression that applies to the full range,

$$\sqrt{w'} = f \left(1 + \sqrt{1 - \frac{1}{f^2}} \right), \quad (15)$$

where the choice of the “plus” root gives the steeper of the two acceleration solutions.

To obtain specific values for the flow speed, we can numerically integrate the scaled equation of motion (12) accounting for the complex functional dependence of the finite-disk factor (eq. [11]) on radius, velocity, and velocity gradient. The left panel in Figure 5 shows how the ratio of terminal to escape speed depends on the CAK power index α ; the right panel plots the full radial variation of velocity for the $\alpha = 0.6$ case. The dashed curves compare results for a similar integration when a canonical β velocity law is used to evaluate

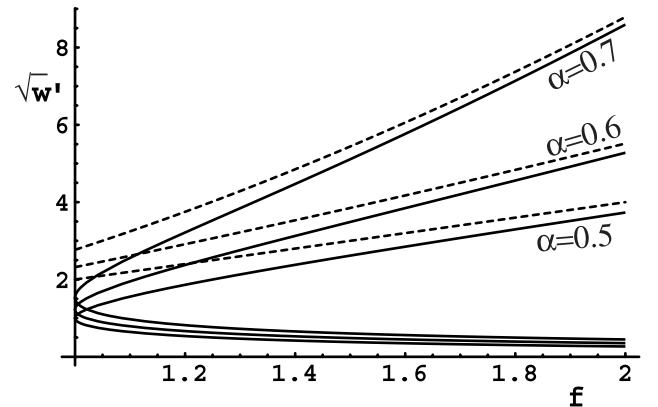


FIG. 4.—Root of the scaled acceleration $\sqrt{w'}$ that solves the equation of motion (12), plotted as a function of the surface-normalized finite-disk factor f . Since the wind terminal speed scales as $v_\infty \sim \sqrt{w'} v_{esc}$, note that even modest increases in the finite-disk factor can lead to a very high speed wind (especially for larger α). The dashed curves denote the asymptotic solutions $\sim (C_c f)^{1/2(1-\alpha)}$ that apply in the limit of large acceleration $w' \gg 1$.

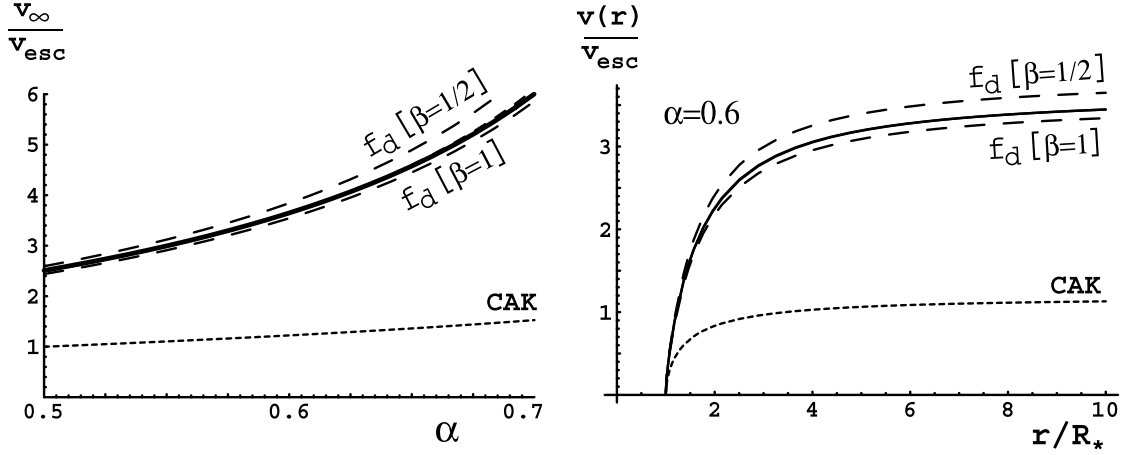


FIG. 5.—Comparison of the full finite-disk solutions (solid curves) with integrations that use a β -velocity law to obtain spatially explicit approximations for the finite-disk factor (dashed curves). *Left*: The ratio of terminal to escape speed vs. CAK exponent α . *Right*: Radial variation of the velocity for the $\alpha = 0.6$ case. In both panels, results for a model using $\beta = \frac{3}{4}$ to evaluate the finite-disk factor are also included but are indistinguishable from the full solution plotted by the solid line. The dotted curves show corresponding results for the point-star CAK model.

the finite-disk factor. For $\beta = 0.75$ the curves are indistinguishable from the full calculation, and other values of β also give very good approximations.

A basic conclusion is thus that one may derive accurate finite-disk-corrected wind solutions using a β velocity law to obtain spatially explicit approximations of the finite-disk factor, with especially good agreement obtained for $\beta \approx 0.75$.

4. THE EFFECT OF NONSPHERICAL AREA EXPANSION

4.1. Kopp-Holzer Expansion in a Point-Star CAK Wind

The above formulation of standard line-driven wind theory provides a convenient basis for understanding the results of models extended to include magnetic fields. As first analyzed by M88, one potentially key effect regards the faster-than-radial expansion of the area in a flow tied to a rapidly diverging magnetic field. Following Kopp & Holzer (1976), it is convenient to consider an infinitesimal flow tube with a nonradial expansion but still with a radial orientation, such as would apply, for example, to flow emanating from the poles of a surface magnetic dipole. The nonradial expansion factor can then be written as

$$h(r) \equiv \frac{A(r)}{A_*} \frac{R_*^2}{r^2} = \frac{B(R_*)}{B(r)} \frac{R_*^2}{r^2}, \quad (16)$$

where the latter equality follows from the $\nabla \cdot \mathbf{B} = 0$ property of any magnetic field, since that then implies $d(BA)/dr = 0$ and so $A \sim 1/B$ along such a radial flow tube.

In the absence of a detailed dynamical solution for the magnetic field divergence, M88 adopted the Kopp & Holzer (1976) phenomenological nonspherical expansion factor,³

$$h_{\text{KH}} = \frac{h_{\text{max}} \exp[(r - R_1)/\sigma] + 1 - (h_{\text{max}} - 1) \exp[(R_* - R_1)/\sigma]}{\exp[(r - R_1)/\sigma] + 1}, \quad (17)$$

³ We use the notation h instead of Kopp and Holzer's f to distinguish from the finite-disk correction defined above.

where R_1 , σ , and h_{max} are free parameters, the first two specifying the location and extent of the nonspherical expansion region and the last fixing the total overall level of nonspherical expansion.

Following M88, we fix sample values of the two Kopp-Holzer parameters, $R_1 = 1.25R_*$ and $\sigma = 0.1$, and compare models with various $h_{\text{max}} = 1.5$ and 2.

Applying this Kopp & Holzer expansion factor to CAK line-driven wind models computed in the idealized point-star approximation, M88 found substantial (more than a factor of 3) increases in wind terminal speed for even modest values of the total nonspherical expansion, $h_{\text{max}} \approx 2$. The above formalism provides a convenient way to understand those results and, indeed, to extend them to account for the combined effects of a nonspherical expansion and a finite-disk correction (see § 4.2). Noting from equation (2) that the line acceleration scales with the density ρ as $g_{\text{CAK}} \sim 1/\rho^\alpha$, we see from the steady state mass conservation relation $\rho \sim 1/vA \sim h(r)/vr^2$ that along a radial flow with nonspherical expansion (“nse”), the line force has the form

$$g_{\text{nse}} = h(r)^\alpha g_{\text{CAK}}. \quad (18)$$

The relevant equation of motion thus takes the same general form as given in equation (12) if we simply replace the finite-disk correction with the nonspherical expansion, $f \rightarrow h^\alpha$. With this redefinition, the dependence of the scaled acceleration w' on h^α is thus again given by Figure 4.

Figure 6a illustrates results for this case, showing the spatial variation (in terms of the inverse radius coordinate x) of $\log w'$ (left) and wind speed ratio $\sqrt{w} = v/v_{\text{esc}}$ (right). (The latter is obtained by straightforward numerical integration of the acceleration w' over x .) In both panels, the dotted and dashed curves represent respectively the point-star and finite-disk solutions for spherical expansion, while the dot-dashed and solid curves represent the corresponding nonspherical solutions for this standard M88 case with $\alpha = 0.7$ and $h_{\text{max}} = 2$. Note that both the acceleration and velocity laws in this point-star, nonspherical expansion case (dot-dashed curve) agree roughly with what is found in the corresponding spherical, finite-disk model (dashed curve). In this sense, the M88 results for this h_{max} can be roughly thought of as simply

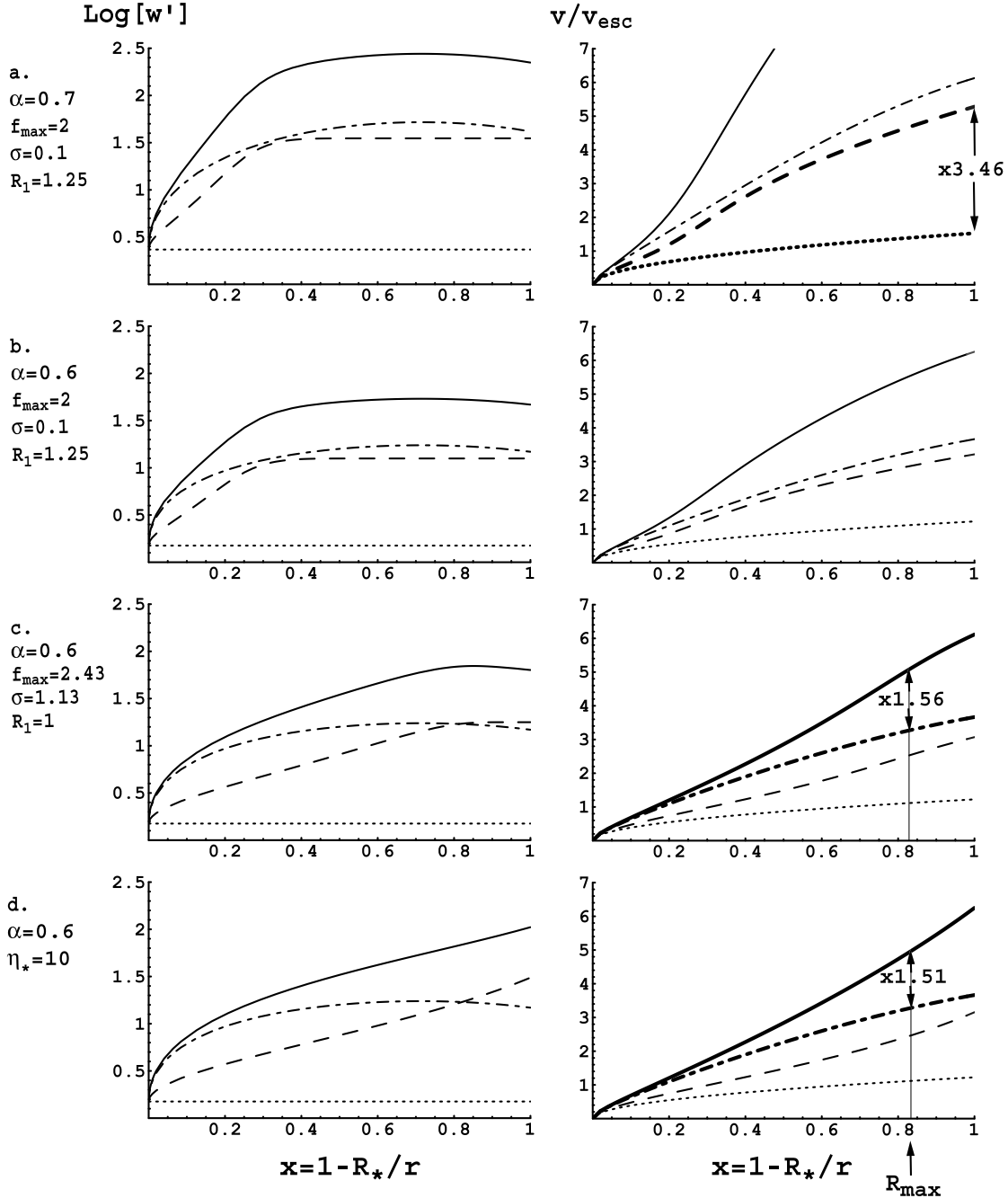


FIG. 6.—Results for various one-dimensional flow models, showing the log of scaled acceleration w' (left) and the ratio of flow speed to escape speed v/v_{esc} (right), plotted vs. scaled inverse radius $x \equiv 1 - R_*/r$. The dotted and dot-dashed curves represent respectively the point-star and finite-disk solutions for spherical expansion, while the dashed and solid curves represent the corresponding nonspherical solutions. Panels *a–d* represent various models, with key parameters as labeled on the left. The top three models (*a–c*) use the Kopp-Holzer scaling in eq. (17), while the bottom model uses the scaling of eqs. (20) and (22), with $\eta_* = 10$.

substituting the nonspherical expansion for the finite-disk correction.

For this case with $h_{\text{max}} = 2$ we find in particular a terminal speed ratio $v_{\infty}/v_{\text{esc}} = 5.2$, which, for the M88 assumed stellar parameters that set the effective escape speed $v_{\text{esc}} = 974 \text{ km s}^{-1}$, yields a terminal speed $v_{\infty} \approx 5145 \text{ km s}^{-1}$, or slightly above the value $v_{\infty} = 4799 \text{ km s}^{-1}$ quoted in Table 1 of M88. (The modest difference is due to the neglect here of gas-pressure terms that were included in M88's more elaborate analysis; see Appendices A and B.) When compared to the terminal speed expected for point-star spherical expansion $v_{\infty} =$

$[\alpha/(1-\alpha)]^{1/2} v_{\text{esc}} = 1.53 \times 974 = 1488$ (which is slightly below the value 1512 km s^{-1} found in M88's solution with gas pressure included), we see that nonspherical expansion with $h_{\text{max}} = 2$ leads to a speed increase of 3.46.

Table 1 summarizes the speed enhancement factors for this case, as well as for a series of other models to be described below. A key point here is that the strong flow speed increases M88 obtained from including nonspherical expansion in the point-star CAK model are quite analogous to the speed increases obtained by including a finite-disk correction. Let us next extend our analysis to include both effects.

TABLE 1
RATIO OF FLOW SPEEDS BETWEEN NONSPHERICAL AND SPHERICAL EXPANSION MODELS

MODEL	$\alpha = 0.5$		$\alpha = 0.6$		$\alpha = 0.7$	
	$r \rightarrow \infty$	$r = 6R_*$	$r \rightarrow \infty$	$r = 6R_*$	$r \rightarrow \infty$	$r = 6R_*$
M88:						
$h_{\max} = 1.5$	1.80	1.94	2.01	2.16	2.39	2.56
$h_{\max} = 2.0$	2.22	2.39	2.62	2.81	3.46	3.69
M88 + f_d :						
$h_{\max} = 1.5$	1.26	1.25	1.37	1.36	1.60	1.58
$h_{\max} = 2.0$	1.47	1.46	1.71	1.69	2.22	2.20
KH + UO02:						
$\eta_* = 0.1$	1.10	1.08	1.13	1.12	1.21	1.19
$\eta_* = 1.0$	1.26	1.23	1.38	1.33	1.65	1.56
$\eta_* = 10$	1.43	1.36	1.67	1.56	2.22	2.01
Eq. (20):						
$\eta_* = 0.1$	1.13	1.11	1.19	1.15	1.29	1.24
$\eta_* = 1.0$	1.26	1.21	1.38	1.30	1.64	1.50
$\eta_* = 10$	1.45	1.34	1.71	1.51	2.33	1.91

NOTES.—The top group of M88 models is based on the CAK point-star model, but all remaining data include the finite-disk correction. The third group uses the Kopp-Holzer nonspherical function (eq. [17]) with parameters set by fits from Fig. 7 of UO02 (see also our Fig. 7), while the bottom group uses eq. (20) with $R_c = \eta_*^{3/8} R_*$. The italics emphasize the strong speed enhancement of the M88 point star model and the more moderate values of the third and fourth model groups. Note the latter agree quite well with the MHD simulation results from Fig. 1b, which give polar speed ratios of 1.12, 1.34, and 1.54 for $\eta_* = 0.1, 1$, and 10.

4.2. Combined Effects of Nonspherical Expansion and a Finite Disk

For a radial flow the combined modification to the line force due to finite disk and nonspherical expansion is given simply by the product of these separate⁴ correction factors,

$$g_{\text{fd,nse}} = f_d h^\alpha g_{\text{CAK}}. \quad (19)$$

We can thus analyze the combined dynamical effect by solving the equation of motion given again by equation (12), applying now the simple substitution $f \rightarrow (f_d/f_*)h^\alpha$. With this combined rescaling, Figure 4 again gives the dependence of $\sqrt{w'}$ on the combined correction factor f .

The solid curves in Figure 6a give the acceleration and velocity for the full solution of combined nonspherical expansion plus finite disk. Compared to the above point-star case, note that the acceleration is now very strong, with indeed the velocity in this case going off the scale, approaching an extraordinarily large terminal speed $v_\infty = 13.6v_{\text{esc}} = 13,255 \text{ km s}^{-1}$! However, note that even the spherical, finite-disk model in this case also has a very large terminal speed of $v_\infty = 6.13v_{\text{esc}} = 5971 \text{ km s}^{-1}$. As such, in *relative* terms of nonspherical to spherical enhancement, the finite-disk case implies a terminal speed factor of “only” 2.22, which is actually significantly less than the factor 3.46 of the M88 point-star assumption for this case.

Nonetheless, in *absolute* terms the implied terminal speeds well in excess of $10,000 \text{ km s}^{-1}$ in such a model are several times higher than the fastest speeds (ca. 5000 km s^{-1}) inferred from blue edges of the P Cygni wind lines from “normal” OB stars (Prinja & Howarth 1986; Howarth & Prinja 1989). In this sense, if finite-disk effects had been included in M88’s original analysis, the implications of assuming hot-star magnetic fields

would have seemed even more dramatic; indeed, the lack of observational evidence for such high speeds may well have been interpreted as strong evidence against existence of a dynamically significant magnetic field (i.e., with confinement parameter $\eta_* > 0.1$).

But now, with the benefit of the full MHD simulations of UO02, we have a strong incentive to investigate the situation further, and indeed the simple formalism here makes it possible to readily examine the effect of varying parameters, as summarized in Table 1.

4.2.1. Effect of More Modest CAK Exponent α

The analysis in § 3 and particularly the results in Figures 4 and 5 suggest that a key parameter in influencing the wind flow speed is the CAK power index α . Thus, in comparing the M88 results with those of the UO02 MHD simulations, it is important to note that the former assumed $\alpha = 0.7$ and the latter $\alpha = 0.6$.

Figure 6b thus provides results for the same Kopp-Holzer parameters as used in M88 (and in Fig. 6a), but now with $\alpha = 0.6$. Note that the accelerations and speeds are all reduced. In particular, the case with nonspherical expansion combined with finite disk now has a terminal speed of $v_\infty = 6.28v_{\text{esc}} = 6113 \text{ km s}^{-1}$, representing a more modest factor 1.71 enhancement over the terminal speed $v_\infty = 3.67v_{\text{esc}} = 3570 \text{ km s}^{-1}$ of the corresponding spherical, finite-disk model.

4.2.2. Using Dynamically Motivated Values for the Kopp-Holzer Parameters

To further facilitate comparisons with our MHD simulations results, let us next consider Kopp-Holzer parameter values that are adjusted to fit the nonspherical expansion found in these simulations. Using equation (16) to convert magnetic field variations into flow area, Figure 7 plots the radial variation of the polar expansion factor found in the MHD simulations assuming various magnetic confinement parameters η_* . The dashed curve shows the expected result for a pure dipole in the limit of a large confinement parameter, $\eta_* \rightarrow \infty$. The lower,

⁴ Actually, a faster-than-radial expansion generally also implies a larger lateral velocity gradient and thus alters the finite-disk correction factor from its usual spherical form (eq. [11]). In practice, we find this to be a minor correction, except very near the stellar surface, where it leads to a slightly increased mass-loss rate. See Appendix B.

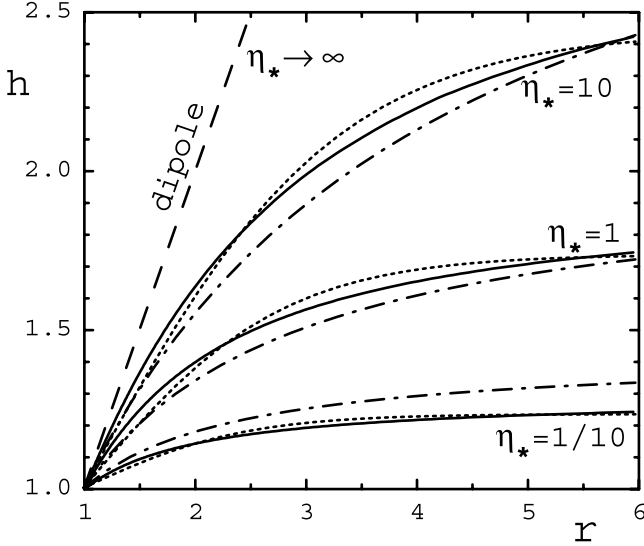


FIG. 7.—Nonspherical expansion factor $h(r)$ for polar flow from full MHD simulations of UO02, plotted vs. radius for magnetic confinement parameters $\eta_* = 1/10, 1$, and 10 (solid curves). The dotted curves compare the best-fit Kopp-Holzer parameterizations, quoted in Fig. 7 of UO02 as respectively $h_{\max} = 1.23, 1.73$, and 2.43 and $\sigma/R_* = 0.73, 0.89$, and 1.13 , with $R_1 = R_c$ in all cases. The dot-dashed curves here add the simple physical fit form of eqs. (20) and (22). The dashed curve shows the expected result for a pure dipole in the limit of a large confinement parameter, $\eta_* \rightarrow \infty$.

middle, and upper solid curves show the MHD results for $\eta_* = 0.1, 1$, and 10 . The dotted curves plot the best-fit Kopp-Holzer parameterizations, quoted in Figure 7 of UO02.

For the Kopp-Holzer fit to the strongest confinement case $\eta_* = 10$, Figure 6c shows that the enhancements in acceleration and speed are again quite modest. Indeed, at the radius $R_{\max} = 6R_*$ of the outer boundary of the UO02 MHD simulation, the speed of this one-dimensional model is $v_6 = 5.72v_{\text{esc}} = 5576 \text{ km s}^{-1}$. Relative to the speed of the spherical case at this radius, $v_6 = 3.29v_{\text{esc}} = 3200 \text{ km s}^{-1}$, this represents an enhancement factor of about 1.56, which is now remarkably close to the factor ~ 1.54 found for the polar flow of the two-dimensional MHD model (cf. Fig. 1b).

Table 1 shows similarly good agreement between this modified Kopp-Holzer parameterization and the MHD simulations (Fig. 1b) that show polar speed enhancements of about 1.12 and 1.32 for confinement parameters $\eta_* = 0.1$ and 1 .

4.3. A Dynamically Motivated Nonspherical Expansion Function

The overall variation of the MHD nonspherical expansion factors plotted in Figure 7 (and in Fig. 7 of UO02) suggests a simpler, more physically motivated fitting function,

$$h_{\text{UO}}(r) = \frac{r}{R_*} \frac{R_* + R_c}{r + R_c}, \quad (20)$$

which has just a single parameter R_c representing a “magnetic confinement radius.” This characterizes the transition between the dipole scaling $h \sim r$ that applies for a strong field near the surface and the asymptotic monopole scaling $h \rightarrow \text{constant}$ that applies at large radii, where the wind has stretched the field into a nearly radial configuration. Note that in the opposite limits $R_c \rightarrow 0$ or $R_c \rightarrow \infty$, the monopole or dipole scalings apply

throughout the flow, as appropriate to the limits of weak ($\eta_* \rightarrow 0$) or strong ($\eta_* \rightarrow \infty$) magnetic confinement.

This suggests a direct scaling of R_c with the confinement parameter η_* . In general, the ratio of magnetic energy to wind kinetic energy should scale as $\eta(r) = \eta_*(r/R_*)^{2-2p}$, where $B(r) \sim 1/r^p$, with $p = 3$ for a dipole and $p = 2$ for a monopole. If we then assume that the confinement radius occurs where this ratio has some order-unity value η_c , we obtain a general scaling of the form

$$\frac{R_c}{R_*} \approx \left(\frac{\eta_*}{\eta_c} \right)^q, \quad (21)$$

where $q = 1/(2p - 2)$ should be intermediate between the dipole ($p = 3$) value $q_d = \frac{1}{4}$ and the monopole ($p = 2$) value $q_m = \frac{1}{2}$. Taking the simple case that the order-unity constant η_c is in fact unity, we find quite good fits for an exponent $q = \frac{3}{8}$, representing the “geometric mean” between the dipole and monopole scalings for R_c ,

$$R_c \approx \eta_*^{3/8} R_*. \quad (22)$$

The dot-dashed curves in Figure 7 plot the radial variations of this simple, physically motivated form of the single-parameter nonspherical-expansion function (eq. [20]). Note that the agreement with the corresponding MHD simulation results (solid curves) is almost as good as the best-fit, three-parameter, Kopp-Holzer form (dotted curves; eq. [17]) that has less physical justification.

Figure 6c shows the acceleration and speed when this simple scaling is applied to the strong confinement case with $R_c = 10^{3/8} R_* = 2.37R_*$. At the simulation outer radius $R_{\max} = 6R_*$, the speed enhancement of this nonspherical, finite-disk model is now a factor of about 1.51, which is again remarkably close to the factor ~ 1.54 found for the polar flow of the two-dimensional MHD model (cf. Fig. 1b). Table 1 shows similarly good agreement between this simpler nonspherical enhancement factor and the MHD polar speed enhancements for the other confinement parameter cases.

5. MASS LOSS FOR TILTED FLOW

In addition to modifying the flow divergence, a magnetic field can also alter a flow’s direction. In particular, for a strong field the initial flow off the stellar surface occurs at an angle tilted to the local radial direction. In this section we examine how such a base flow tilt should influence the local mass flux.

Since the mass loss is set very near the stellar surface, where the combined factor from nonspherical divergence and finite-disk correction has its minimum, let us ignore both sphericity and magnetic divergence effects and consider the field and flow to be along a *fixed* direction \hat{s} , assumed to be tilted by an angle θ_B with respect to the local vertical direction, defined by unit vector \hat{z} . We then have $\mu_B \equiv \cos \theta_B = \hat{s} \cdot \hat{z}$, and in terms of the local horizontal direction \hat{x} , we can also write $\hat{s} = \mu_B \hat{z} + (1 - \mu_B^2)^{1/2} \hat{x}$.

For our usual simplification of negligible gas pressure, the steady state equation of motion along the fixed field direction \hat{s} becomes (cf. eq. [1])

$$(\mathbf{v} \cdot \nabla)(\hat{s} \cdot \mathbf{v}) = -g_*(\hat{s} \cdot \hat{z}) + \hat{s} \cdot \mathbf{g}_{\text{CAK}}, \quad (23)$$

where on the right-hand side \mathbf{g}_{CAK} represents the vector radiative force and we have used the fact that surface gravity

$g_* \equiv (1 - \Gamma)GM/R_*^2$ is along the local vertical \hat{z} . On the left-hand side the advective derivative of velocity along \hat{s} can be written as

$$\begin{aligned} (\mathbf{v} \cdot \nabla)(\hat{s} \cdot \mathbf{v}) &= v_s(\hat{s} \cdot \mathbf{v})(v_s) \\ &= \mu_B v_s \frac{\partial v_s}{\partial z} + \sqrt{1 - \mu_B^2} v_s \frac{\partial v_s}{\partial x} \\ &= \mu_B v_s \frac{\partial v_s}{\partial z}, \end{aligned} \quad (24)$$

where the last expression assumes that there are no horizontal variations in velocity.

For the line-driving, let us again assume a point-source approximation with the radiation confined to a pencil beam along the local vertical \hat{z} . In terms of an associated surface flux $F_* \equiv L/4\pi R_*^2$, the projected CAK line-force term then becomes (cf. eq. [2])

$$\begin{aligned} \hat{s} \cdot \mathbf{g}_{\text{CAK}} &= \frac{1}{1 - \alpha} \frac{\bar{Q} \kappa_e F_*}{c} (\hat{s} \cdot \hat{z}) \left[\frac{\hat{z} \cdot \nabla(\hat{z} \cdot \mathbf{v})}{\bar{Q} \kappa_e \rho c} \right]^\alpha \\ &= \frac{\mu_B}{1 - \alpha} \frac{\bar{Q} \kappa_e F_*}{c} \left(\frac{\mu_B \partial v_s / \partial z}{\bar{Q} \kappa_e \rho c} \right)^\alpha \\ &= \frac{\mu_B}{1 - \alpha} \frac{\bar{Q} \kappa_e F_*}{c} \left(\frac{\mu_B v_s \partial v_s / \partial z}{\bar{Q} \kappa_e \dot{m}_s c} \right)^\alpha \\ &= \frac{\mu_B}{1 - \alpha} \frac{\bar{Q} \kappa_e F_*}{c} \left(\frac{\mu_B^2 v_s \partial v_s / \partial z}{\bar{Q} \kappa_e \dot{m}_r c} \right)^\alpha, \end{aligned} \quad (25)$$

where the third equality uses mass conservation along the tilted flow to eliminate the density ρ in favor of the mass flux in the tilted direction, $\dot{m}_s \equiv \rho v_s$. The final equality then uses the fact that the associated *radial* mass flux component \dot{m}_r (which sets the associated mass loss through the spherical surface) is reduced by another factor μ_B ; i.e., $\dot{m}_r = \mu_B \dot{m}_s$. After dividing through by μ_B and making the modified definition (cf. eq. [3])

$$w' \equiv \frac{v_s dv_s / dz}{g_*}, \quad (26)$$

the momentum equation (23) can again be recast into the familiar form (cf. eq. [4])

$$w' = -1 + C \mu_B^{2\alpha} (w')^\alpha, \quad (27)$$

where C is defined in equation (5) and is related to the maximal value of the radial mass flux. Equation (27) is mathematically identical to equation (4) under the substitution $C \rightarrow C \mu_B^{2\alpha}$. As such, following the same procedure as in § 3.1, we find that the surface mass flux scales as

$$\dot{m}_r = \mu_B^2 \dot{m}_{\text{CAK}}, \quad (28)$$

where $\dot{m}_{\text{CAK}} \equiv \dot{M}_{\text{CAK}}/4\pi R_*^2$ is the analogous surface mass flux in the CAK model for spherical mass loss.

The μ_B^2 reduction of the radial surface mass flux predicted by this simplified planar, one-dimensional flow analysis is actually in quite good agreement with the results of our full two-dimensional MHD simulations (ud-Doula 2002; UO02). Indeed, the solid curves of Figure 1a show that the mass flux scaled by μ_B^2 is roughly constant in latitude and equal to the mass flux in the spherical case. Physically, one factor of μ_B can be attributed simply to geometric projection of the tilted flow

onto the vertical normal to the star's spherical surface, while the other can be seen to result from the tilted flow acceleration having less effect in desaturating the optically thick absorption of the radially streaming radiation.

This lower initial mass flux combined with the faster-than-radial area expansion leads to a lower density, which through the CAK line force leads to a greater acceleration and thus a faster terminal speed. In cases with a large magnetic confinement parameter (i.e., $\eta_* = 10$), the simulations thus tend to show the greatest terminal speeds at latitudes just away from the magnetic equator, which originate from the open field lines that are farthest from the magnetic pole and for which the initial flow tilt at the surface wind base is greatest (see our Fig. 1b and the right panel of Fig. 8 in UO02).

6. DISCUSSION

The mass flux and speed variations arising in such magnetic models of line-driven winds provide a potentially attractive mechanism for explaining the extensive wind structure and variability commonly inferred from observations of UV P Cygni lines from OB stars (e.g., Kaper et al. 1996; Prinja et al. 1998). If the models here were extended to include even a modest stellar rotation along an axis that is *tilted* relative to the magnetic dipole axis, then the speed variations with magnetic latitude would naturally lead to corotating interaction regions (CIRs), much as occur between faster and slower streams in the solar wind. Following initial suggestions by Mullan (1984), such CIRs now represent a popular general paradigm for explaining the commonly observed “discrete absorption components” (DACs) in P Cygni absorption troughs. But in previous hydrodynamic simulations by Cranmer & Owocki (1996), the speed variations leading to CIR formation had to be induced somewhat artificially by assuming a modulation of the base wind-driving, as might result from, e.g., bright or dark spots on the stellar surface. Since the analyses here (and the UO02 MHD simulations) show that even modest magnetic confinement parameters can lead to quite substantial latitudinal variations in flow speed, a tilted dipole field seems a much more likely mechanism for inducing such wind CIRs.

Note that such CIRs would also tend to limit the highest speeds occurring from the most rapidly diverging flow, simply from the truncation by the interaction with the slower speed flow. As such, the cases with the highest overall flow speeds would be those with a strong, *rotation-aligned* dipole, for which the high-speed polar wind would not be brought into interaction with the slower, equatorial wind. Such cases may be relatively rare, but they are possible. The flow speeds would be quite high, perhaps up to twice that of a spherical wind. But the analysis here shows that they need not be absurdly high, at least for moderate values of the CAK power index, i.e., $\alpha \approx 0.6$.

7. CONCLUDING SUMMARY

This paper analyzes the effects of the flow tilt and non-spherical expansion associated with magnetic channeling on the mass flux and flow speeds of a line-driven stellar wind. Our main results are summarized as follows:

1. A faster-than-radial expansion leads to an enhancement in wind speed, but the relative corrections are typically about 50% when compared with a finite-disk-corrected model with a moderate CAK power index $\alpha = 0.6$, much less than the factor of 3 or more inferred by M88 in their analysis of a point-star model with $\alpha = 0.7$. The analysis here is in good

quantitative agreement with results from numerical MHD simulations.

2. The nonradial expansion obtained from our numerical MHD models differs from the heuristic form used by Kopp & Holzer (1976), with the rapid expansion beginning right at the wind base and extending over a quite large radial distance. We propose a simpler, physically motivated fit function (eq. [20]) controlled by a single parameter R_c , which represents a characteristic radius for wind magnetic confinement and scales as $R_c \sim \eta_*^{3/8}$ with the magnetic confinement parameter $\eta_* (\equiv B_{\text{eq}}^2 R_*^2 / \dot{M} v_\infty)$.

3. The radial mass flux at the stellar surface with a tilted magnetic field is reduced by the square of the cosine of the tilt angle (μ_B^2), compared with a nonmagnetic, spherical wind. Physically, one factor of μ_B stems from the geometric projection of the tilted flow onto a surface normal, while the other arises from the reduced desaturation of absorption of radially streaming radiation by acceleration along this tilted flow.

4. A perturbation analysis (in Appendices A and B) shows that the corrections from a small but nonzero gas pressure scale with the ratio of sound speed to escape speed, a/v_{esc} . Relative to a zero-sound-speed, finite-disk-corrected spherical wind, typical increases in the mass-loss rate are 10%–20%, with

comparable relative decreases in the wind terminal speed. In nonspherical models, the additional gas-pressure correction is typically just 1%–2%.

Overall, the results confirm that even modest magnetic fields can have a substantial influence in line-driven winds, with faster areal divergence enhancing the wind acceleration and flow speed. But even the largest inferred enhancements still generally allow for speeds that are within the range of observational constraints. As such, strong magnetic fields in hot-star winds should not be precluded, as they might have been if previous analyses implying large speed enhancements had not been reduced by the more complete study here.

This research was supported in part by NSF grant AST 00-97983, NASA grants NAG5-11886 and NAG5-11095, and the NASA Space Grant College program at the University of Delaware. S. P. O. acknowledges support of a PPARC visiting fellowship and thanks J. Brown of the University of Glasgow and A. Willis of University College London for their hospitality during his sabbatical-year visits. We thank R. Townsend and D. Cohen for helpful discussions and comments.

APPENDIX A

NONZERO-SOUND-SPEED CORRECTION FOR A SPHERICAL, FINITE-DISK MODEL

Let us examine here the effect of a finite gas pressure associated with a nonzero sound speed. In the zero-sound-speed limit considered in §§ 3–5, the minimal value of the finite-disk correction factor $f_{d*} = 1/(1 + \alpha)$ occurring near the stellar surface, $r \rightarrow R_*$, sets the critical conditions that determine the maximal allowed steady mass-loss rate \dot{M}_{fd} . But with a finite sound speed, the reduced effective inertia $(1 - s/w)w'$ in the base region near the sonic point shifts this critical location for the most difficult driving slightly away from the surface wind base. But then, because of the somewhat larger finite-disk factor, this in turn allows a somewhat larger maximal mass-loss rate.

To analyze these effects, let us recast the equation of motion in the form

$$F(x, w, w') \equiv \left(1 - \frac{s}{w}\right)w' + 1 - \frac{f}{(1 + \delta m_s)^\alpha} C_c(w')^\alpha - \frac{2s}{1 - x} = 0, \quad (\text{A1})$$

where $s \equiv (a/v_{\text{esc}})^2$ is typically of order 10^{-3} and

$$\delta m_s \equiv \frac{\dot{M}_{\text{fd,fs}}}{\dot{M}_{\text{fd}}} - 1 \quad (\text{A2})$$

is the fractional correction of the mass-loss rate due to this small but nonzero s . The new critical point where this mass loss is fixed now occurs somewhat away from the surface, $x_c > 0$, but in the usual cases where $s \ll 1$, we expect both $\delta m_s \ll 1$ and $x_c \ll 1$.

In the narrow region from the sonic point to this critical point, the driving is dominated by the need to overcome gravity. This implies an outward acceleration that scales as the inward gravity, namely, $w'(x) \approx w'_c = \alpha/(1 - \alpha)$, which in turn implies that the velocity in this initial region nearly follows the standard CAK ($\beta = \frac{1}{2}$) solution, $w(x) \approx w'_c x$. Using this, we obtain a spatially explicit form for the finite-disk factor, which upon expansion to first order in $x \leq x_c \ll 1$ becomes

$$f(x) \approx 1 + 4x. \quad (\text{A3})$$

We then find that the equation of motion (A1) takes the spatially explicit form

$$F(x) = \frac{(1 - \alpha)s}{x} + 4x - \alpha \delta m_s + 2s = 0, \quad (\text{A4})$$

where we have also expanded $1/(1 + \delta m_s)^\alpha$ and kept terms to first order in the smallness parameter s . The critical point is located where this function has a spatial minimum,

$$0 = \left(\frac{dF}{dx}\right)_c = 4 - \frac{(1 - \alpha)s}{x_c^2}, \quad (\text{A5})$$

which solves to

$$x_c \approx \frac{\sqrt{(1-\alpha)s}}{2}. \quad (\text{A6})$$

Applying this in equation (A4) and keeping only the leading term of order \sqrt{s} , we find that the mass-loss correction is given by

$$\delta m_s \approx \frac{4\sqrt{1-\alpha}}{\alpha} \frac{a}{v_{\text{esc}}}. \quad (\text{A7})$$

Beyond this critical point, the increase in the finite-disk factor means that solutions to the equation of motion quickly approach their large gradient limit, $w^{1-\alpha} \approx fC^c/(1+\delta m_s)^\alpha$ (see dashed curves in Fig. 4). Since the wind terminal speed scales as $v_\infty \sim \sqrt{w'}$, this implies that the fractional speed corrections from a finite sound speed should scale as

$$\delta v_{\infty,s} \equiv \frac{v_{\infty,s}}{v_{\infty,s=0}} - 1 \approx (1+\delta m_s)^{-\alpha/2(1-\alpha)} - 1 \approx \frac{-\alpha\delta m_s}{2(1-\alpha)} \approx \frac{-2}{\sqrt{1-\alpha}} \frac{a}{v_{\text{esc}}}. \quad (\text{A8})$$

For a typical case with $\alpha = \frac{1}{2}$ and $s \equiv (a/v_{\text{esc}})^2 = 0.001$, we find $x_c \approx 0.012$, $\delta m_s \approx 0.18$, and $\delta v_{\infty,s} \approx -0.09$. For the same s but $\alpha = 0.6$, we get $\delta m_s \approx 0.13$ and $\delta v_{\infty,s} \approx -0.10$, while for $\alpha = 0.7$, we find $\delta m_s \approx 0.10$ and $\delta v_{\infty,s} \approx -0.12$. Applying these corrections to the scalings from the zero-sound-speed calculations in § 3 generally gives very good agreement (to about a percent) with the full solutions.

It is worth noting here that even though the corrections for finite gas pressure are modest, they are not, perhaps, as small as one might have expected. That is, even though the ratio of internal energy to escape energy is of order $s = (a/v_{\text{esc}})^2$, the corrections scale with $\sqrt{s} = a/v_{\text{esc}}$. Moreover, this scaling is multiplied by a large coefficient, which stems from the relatively steep increase in the leveraged finite-disk factor, e.g., scaling as $f^{1/\alpha}(x) \approx 1 + 8x$ for $\alpha = \frac{1}{2}$, equivalent to an r^8 dependence on the radius r . As a result, even though the reduced inertia of a mildly supersonic flow leads to only a relatively modest outward shift of the critical point from the stellar surface, the stronger finite-disk factor leads to a stronger radiative driving and thus allows a larger mass loss. Finally, that larger mass loss also implies a comparable relative reduction in the wind terminal speed.

APPENDIX B

NONZERO-SOUND-SPEED CORRECTION FOR A NONSPHERICAL, FINITE-DISK MODEL

In the case of nonspherical expansion, the analysis follows much as above, except that now we must include the nonspherical expansion factor $h(x)$. In the region near and below the critical point $x \leq x_c \ll 1$, this expands to

$$h(x) \approx 1 + h'_0 x, \quad (\text{B1})$$

where, for the form defined in equation (20),

$$h'_0 = \frac{R_c}{R_* + R_c} \approx \frac{1}{1 + \eta_*^{-3/8}}. \quad (\text{B2})$$

This nonspherical expansion implies a stronger lateral velocity gradient, and for our assumed velocity-law scaling ($w \sim x$), this can be shown to modify the finite-disk correction expansion (eq. [A3]) near the surface to

$$f_h(x) \approx 1 + (4 + h'_0)x. \quad (\text{B3})$$

Including then also the usual effect of this nonspherical expansion on the density, we make the replacement $f \rightarrow f_h h^\alpha \approx 1 + [4 + (1 + \alpha)h'_0]x$ and thereby find that equations (A4) and (A5) still apply if we simply make the substitution $4 \rightarrow 4 + (1 + \alpha)h'_0$. The critical point thus now occurs at

$$x_c \approx \sqrt{\frac{(1-\alpha)s}{4 + (1+\alpha)h'_0}}, \quad (\text{B4})$$

while the mass-loss correction is now given by

$$\delta m_s \approx \frac{2}{\alpha} \sqrt{(1-\alpha)[4 + (1+\alpha)h'_0]} \frac{a}{v_{\text{esc}}} \quad (\text{B5})$$

and the speed correction by

$$\delta v_{\infty, s} \approx \frac{-4}{\sqrt{(1-\alpha)[4+(1+\alpha)h'_0]}} \frac{a}{v_{\text{esc}}}. \quad (\text{B6})$$

For the weak, moderate, and strong magnetic confinement cases ($\eta_* = 0.1, 1$, and 10), we find $h'_0 \approx 0.3, 0.5$, and 0.7 . For the typical s of order 10^{-3} , we find the *extra* changes from nonspherical divergence range from 1% to 2% in both the mass-loss rate and flow speed. In particular, applying the parameters $s = 0.0014$ and $\alpha = 0.6$ used in the UO02 MHD simulations, we estimate extra mass-loss enhancements for the weak-, moderate-, and strong-field cases to be respectively 0.9%, 1.5%, and 2.1%. These values are roughly consistent with the polar mass fluxes plotted in Figure 1a.

REFERENCES

- | | |
|--|--|
| Castor, J. I., Abbott, D. C., & Klein, R. I. 1975, ApJ, 195, 157 (CAK) | MacGregor, K. B. 1988, ApJ, 327, 794 (M88) |
| Cranmer, S. R., & Owocki, S. P. 1996, ApJ, 462, 469 | Mullan, D. J. 1984, ApJ, 283, 303 |
| Feldmeier, A., Shlosman, I., & Hamann, W. 2002, ApJ, 566, 392 | Pauldrach, A., Puls, J., & Kudritzki, R. P. 1986, A&A, 164, 86 |
| Friend, D. B., & Abbott, D. C. 1986, ApJ, 311, 701 | Prinja, R. K., & Howarth, I. D. 1986, ApJS, 61, 357 |
| Gayley, K. G. 1995, ApJ, 454, 410 | Prinja, R. K., Massa, D., Howarth, I. D., & Fullerton, A. W. 1998, MNRAS, 301, 926 |
| Howarth, I. D., & Prinja, R. K. 1989, ApJS, 69, 527 | ud-Doula, A. 2002, Ph.D. thesis, Univ. Delaware |
| Kaper, L., Henrichs, H. F., Nichols, J. S., Snoek, L. C., Volten, H., & Zwarthoed, G. A. A. 1996, A&AS, 116, 257 | ud-Doula, A., & Owocki, S. P. 2002, ApJ, 576, 413 (UO02) |
| Kopp, R. A., & Holzer, T. E. 1976, Sol. Phys., 49, 43 | |